In vivo near-infrared imaging using ternary selenide semiconductor nanoparticles with uncommon crystal structure

Jingke Yao, José Lifante, Paloma Rodríguez, María de la Fuente-Fernández, Francisco Sanz-Rodríguez, Dirk H. Ortgies, Erving Ximendes, Daniel Jaque,* and Riccardo Marin*

Jingke Yao, José Lifante, Dr. Paloma Rodríguez, Dr.Francisco Sanz-Rodríguez, Dr. Dirk H. Ortgies, Dr.Erving Ximendes, Prof. Daniel Jaque,* Dr. Riccardo Marin.
Nanomaterials for Bioimaging Group (NanoBIG), Facultad de Ciencias, Universidad Autónoma de Madrid, C/ Francisco Tomás y Valiente 7, Madrid 28049, Spain
E-mail: daniel.jaque@uam.es and riccardo.marin@uam.es

José Lifante, Dr. Francisco Sanz-Rodríguez, Dr. Dirk H. Ortgies, Dr. Erving Ximendes, Prof. Daniel Jaque.
Nanomaterials for Bioimaging Group (NanoBIG), Instituto Ramón y Cajal de Investigación, Sanitaria Hospital Ramón y Cajal, Ctra. De Colmenar Viejo, Km. 9100, 28034 Madrid, Spain

María de la Fuente-Fernández
Nanomaterials for Bioimaging Group (NanoBIG), Departamento de Fisiología, Facultad de Medicina, Universidad Autónoma de Madrid, C/ Francisco Tomás y Valiente 7, Madrid 28049, Spain

In vivo near-infrared imaging using ternary selenide semiconductor nanoparticles with uncommon crystal structure.

Jingke Yao, José Lifante, Paloma Rodríguez, María de la Fuente-Fernández, Francisco Sanz-Rodríguez, Dirk H. Ortgies, Erving Ximendes, Daniel Jaque,* and Riccardo Marin*

Jingke Yao, José Lifante, Dr. Paloma Rodríguez, Dr.Francisco Sanz-Rodríguez, Dr. Dirk H. Ortgies, Dr.Erving Ximendes, Prof. Daniel Jaque,* Dr. Riccardo Marin.
Nanomaterials for Bioimaging Group (NanoBIG), Facultad de Ciencias, Universidad Autónoma de Madrid, C/ Francisco Tomás y Valiente 7, Madrid 28049, Spain
E-mail: daniel.jaque@uam.es and riccardo.marin@uam.es

José Lifante, Dr. Francisco Sanz-Rodríguez, Dr. Dirk H. Ortgies, Dr. Erving Ximendes, Prof. Daniel Jaque.
Nanomaterials for Bioimaging Group (NanoBIG), Instituto Ramón y Cajal de Investigación, Sanitaria Hospital Ramón y Cajal, Ctra. De Colmenar Viejo, Km. 9100, 28034 Madrid, Spain

María de la Fuente-Fernández
Nanomaterials for Bioimaging Group (NanoBIG), Departamento de Fisiología, Facultad de Medicina, Universidad Autónoma de Madrid, C/ Francisco Tomás y Valiente 7, Madrid 28049, Spain

ABSTRACT

The implementation of *in vivo* fluorescence imaging as a reliable diagnostic imaging modality at the clinical level is still far from reality. A lot of work remains ahead to provide medical practitioners with solid proof of the potential advantages of this imaging technique over well-established ones such as magnetic resonance imaging or nuclear imaging. To do so, one of the key objectives is to improve the optical performance of dedicated contrast agents, thus improving the resolution and penetration depth achievable with *in vivo* imaging. In the present study, we move along this direction and report on the use of $AgInSe_2$ nanoparticle-based contrast agents (nanocapsules) for fluorescence imaging. The use of a Ag_2Se seeds-mediated synthesis method allows stabilizing an uncommon orthorhombic crystal structure. This structure endows the material with emission in the second biological window (1000-1400 nm), where deeper penetration in tissues is achieved. The nanocapsules, obtained via phospholipid-assisted encapsulation of the $AgInSe_2$ nanoparticles, comply with the mandatory requisites for an imaging contrast agent–colloidal stability and negligible toxicity *in vitro*–and show superior brightness compared with well-established and widely used Ag_2S nanoparticles. Imaging experiments point to the great potential of the novel $AgInSe_2$-based nanocapsules for high-resolution, whole-body *in vivo* imaging. In particular, their extended permancence time within blood vessels make them especially suitable for prolonged imaging of the cardiovascular system.

1. Introduction.

Among other conditions, the prosperity of our society depends on a sustainable health system. To that end, access to diagnostic approaches that are fast, inexpensive, and that minimize the discomfort of the patient is pivotal. Currently available techniques, such as magnetic resonance imaging, X-ray computed tomography, and nuclear imaging, offer ever improving performance, but in turn they require sophisticated equipment and elevated maintenance costs. In recent years, fluorescence imaging (FI) has been emerging as a credible complementary technique to those above mentioned.[1] The advantages of FI reside in the use of non-ionizing radiation, simple and less expensive setups, minimal invasiveness, and real-time image-acquisition capabilities. However, its main limitation is the difficulty in obtaining deep-tissue and high-resolution *in vivo* images owing to the large attenuation of light into tissues.[2] The future application of FI at the clinical level as a viable alternative to conventional imaging techniques for selected applications passes through the development of more efficient detection systems as well as novel contrast agents. In this vein, luminescent nanoparticles (NPs) hold great promise.

In search for the most suitable NP-based contrast agents, it soon became clear that *in vivo* images of the highest quality could be obtained with NPs emitting in the so-called biological transparency windows.[3] These are near-infrared (NIR) spectral ranges where biological tissues are less impervious to the electromagnetic radiation, with NIR-I and NIR-II spanning over the 750-950 nm and 1000-1400 nm ranges, respectively.[4] The latest generation of luminescent NPs employed in FI emit in the NIR-II, wherein the low scattering coefficient and reduced absorption from tissue components result in significantly improved penetration depth and resolution of the fluorescence images.[3b] The use of NPs emitting in the NIR-II has made possible, for example, the acquisition of high-resolution *in vivo* images of the cardiovascular system, anatomical images of animal models, as well as molecular imaging of infarcted heart.[5] Carbon nanotubes, lanthanide-doped NPs, and semiconductor NPs are the most representative

4

FI contrast agents.[6] In fact, many of the most significant advances in NIR-II FI have been obtained with semiconductor NPs made of Ag_2S.[5f, 7]

Ag_2S NPs possess desirable properties like good biocompatibility and physicochemical stability.[8] Nonetheless, their performance is severely limited by their low brightness, which stems from low photoluminescence quantum yield (PLQY; $< 0.1\%$ for commercially available Ag_2S), and limited molar absorption coefficient ($4 \cdot 10^{-5}$ M^{-1} cm^{-1} at 800 nm, an optimal excitation wavelength for *in vivo* FI).[9] Moreover, methods to increase their optical performance are scarce, could require special equipment, and often afford limited improvement.[9a, 10] Therefore, the development of NIR-II-emitting semiconductor NPs that are brighter is an urgent matter. $AgInSe_2$ (AISe) NPs, for instance, offer the possibility of achieving large brightness compared with Ag_2S NPs, owing to their higher ($> 20\%$) PLQY and their good photostability.[11] Their ternary nature also allows to finely manipulate their composition via selective cation exchange.[12] However, to the best of our knowledge, AISe NPs have been investigated only once as *in vivo* FI contrast agents by D. Deng *et al.*, who performed tumor imaging using RGD-peptide-decorated AISe/ZnS core/shell NPs.[13] In that study, AISe NPs have their emission centered at 800 nm, imposing the use of an excitation wavelength lying outside of the biological windows (660 nm). Thus, the authors obtained *in vivo* fluorescence images of limited resolution. Being able to push the operating range of AISe NPs into NIR-I and NIR-II, in terms of excitation and emission respectively, would allow achieving images of much higher quality.

To address this issue, in this work we take advantage of a synthesis method that affords AISe NPs with an uncommon crystal structure, which in turn leads to a NIR-II-centered emission. The hydrophobic NPs are transferred to aqueous milieus by encapsulating them in a phospholipid layer. These colloidally stable nanocapsules (NCs) are tested for their toxicity *in vitro* and later utilized as contrast agents for *in vivo* FI. The comparison of the results obtained with AISe NCs and commercial Ag_2S NPs underscores the excellent performance of the newly

developed contrast agents particularly for the visualization of the vasculature, opening the door to further studies on the use of this material for FI.

2. Results and discussion.

The synthesized AISe NPs showed a triangular shape in TEM images, which is suggestive of a tetrahedral habit, and an average size of (8 ± 2) nm (**Figure 1A** and **S1**). They could be easily dispersed in non-polar organic solvents such as TCE, giving an optically clear dispersion (**Figure 1B**). The diffraction pattern of AISe NPs featured broad reflections characteristic of nanometric crystalline domains (**Figure 1C**). Both the morphology and the diffraction pattern were consistent with the data reported by Langevin et al.[14] It is worth noting that these AISe NPs possess an unusual orthorhombic crystalline phase that was first reported by Vittal and co-workers.[15] rather than the most common tetragonal polymorph.[16] The reason for this has to be searched in the NP formation mechanism, which entails orthorhombic Ag_2Se seeds as an intermediate. The subsequent cation exchange with In^{3+} yields $AgInSe_2$ that are isostructural to $AgInS_2$ crystallized in the orthorhombic *Pna*2_1 space group.[14] Therefore, the crystal structure of AISe NPs has memory of the structure of parent Ag_2Se seeds. This uncommon crystal structure is likely the responsible for the unique optical properties of these NPs (*vide infra*). Upon transfer to aqueous media with the aid of phospholipids (**Figure 1D**), the $AgInSe_2$ NPs arranged in quasi-spherical aggregates (**Figure 1A**, right). These nanocapsules form due to two competitive hydrophobic interactions: i) between DDT molecules attached to the surface of the NPs and the hydrophobic tail of the phospholipids, ii) between DDT molecules on the surface of different NPs. The stability of the AISe NCs in aqueous media was confirmed by DLS measurements, which showed a sizeable increase of the effective diameter when passing from tetrachloroethylene (TCE) to phosphate buffer saline (PBS) 1x (**Figure 1E**, left). We further tested the colloidal stability of the AISe NCs in PBS over the 15-55 ºC temperature range (**Figure 1E**, middle), observing negligible changes in the hydrodynamic diameter

(approximately 150 nm; Z-average) and in the polydispersion index (PDI; approximately 0.2). As expected, the measured Z-potential was negative (-33 mV), due to the partial hydrolyzation of the maleimide groups on the surface of AISe NCs (**Figure 1E**, right).[17] This hydrolyzation ultimately resulted in the appearance of carboxylic groups, whose deprotonation in aqueous media leads to an overall negative surface charge. The use of phospholipids with maleimide was preferred due to the documented increased interaction of nanoparticles featuring this functional group towards cellular thiols (*vide infra*).[18] To further confirm the presence of phospholipids on the surface of the NCs, FTIR spectra of the as-synthesized AISe NPs and AISe NCs were collected and compared with the spectra of pristine organic molecules (**Figure 1F**). Upon encapsulation of the AISe NPs in phospholipids, the signals originating from DSPE-PEG$_{2000}$-MAL became dominant over those coming from DDT, thus confirming the presence of amphiphilic molecules in the NCs. We then tested the cytotoxicity of AISe NCs, incubating HeLa cells at different concentrations (5-100 μg/mL) for 2 and 24 h (**Figure 1G**). The results did not indicate appreciable toxicity, with a maximum cell viability decrease of 13% after 2 h of incubation at an AISe NCs extracellular concentration of 100 μg/mL. The absence of cell toxicity of our NCs is in agreement with previous works reporting good biocompatibility of AgInSe$_2$ NPs against cancerous and normal cell lines.[19] Altogether, the observed excellent colloidal stability in PBS along with the lack of substantial toxicity indicated the amenability of the developed NCs to applications in the biomedical context.

Subsequently, the optical properties of the material were assessed. As can be observed in **Figure 2A**, while the extinction spectrum is not affected by the dispersing solvent, AISe NCs in water exhibited an emission that is slightly blue-shifted and narrower compared to the one of parents AISe NPs dispersed in TCE. This change in the emission spectral profile could be mainly attributed to the prominent inner filter effect exerted by water, which has strong absorption bands in the wavelength range of interest. [20] As expected, the transfer to water induces a sizeable intensity decrease close to 80% (**Figure S2**), which is attributed to the

activation of non-radiative de-excitation events involving water vibrations.[21] To benchmark the brightness of AISe NCs, we compared their optical properties with those of commercial Ag_2S NPs (**Figure 2B-D**). NIR images acquired under 800-nm excitation with the *in vivo* optical setup (see Experimental Section) show that AISe NCs have a much brighter luminescence compared with Ag_2S NPs (**Figure 2B**).

Upon integrating the emission spectra acquired on these dispersions (**Figure 2B**), we estimated that our AISe NCs are approximately 7.5 times brighter than Ag_2S NPs under our experimental conditions. The molar extinction coefficient (ε) of AISe NCs was calculated to be roughly 3.5 times smaller than the one Ag_2S NPs (**Figure 2D**; see also Supporting Information for detail around these calculations). Therefore, since the brightness is defined as the product between ε and PLQY, according to the above observations the PLQY of AISe NCs should be approximately 25 times larger than the one of Ag_2S NPs. Considering a value of 0.1% for Ag_2S NPs,[22] this translates to a PLQY of 2.5% for AISe NCs. This value well agrees with an estimate of 3.5%, based on the 21% PLQY reported by Langevin et al. for AISe NPs in TCE[14] and an 80% intensity loss observed when passing from TCE to water (**Figure S2**). Admittedly, optimization of the reaction conditions[10] or use of ultrafast photochemistry methods[23] allows producing Ag_2S NPs whose PLQY is on par or higher than the values herein reported for AISe NCs. However, we should point out that our synthesis protocol did not undergo any optimization. Therefore, it is expected that further adjustment of the synthesis conditions and, possibly, exploitation of selective cation exchange[12] could push the brightness of AISe NCs to even higher values.

To complete the characterization of our AISe NCs, we also investigated the temperature dependence of their photoluminescence. As described in detail in the Supporting Information (**Figure S3**), the thermal sensitivities retrieved for intensity- and lifetime-based thermometric approaches were 4.5 and 3% ºC^{-1} respectively at 37 ºC. These numbers are similar to those reported previously for Ag_2S NP-based luminescent thermometers used for *in vivo* thermal

sensing.[7b, 7d, 24] Moreover, as demonstrated above, AISe NCs are brighter and should therefore provide higher spatiotemporal resolutions. Thus, although the use of AISe NCs as thermal sensors lies outside the scope of this study, these nanoprobe hold great potential as biocompatible luminescent thermometers.

Encouraged by the low toxicity and high brightness of our NPs, we moved to *in vivo* measurements (**Figure 3**). We administered 150 µL of a 1.0-mg/mL dispersion of either AISe NCs or commercial Ag_2S NPs in PBS 1x to two female CD1 mice via retro-orbital injection. and monitored the evolution of the NIR signal over the course of 3 h under 808-nm excitation (**Figure 3A**). From the comparison of the NIR-II images obtained at different timepoints, it is apparent how the higher brightness of AISe NCs translates to an improvement in image contrast and resolution. When using AISe NCs, the vasculature of the animal became visible and remained distinguishable throughout the whole timespan of the measurements (albeit with a partial loss of overall intensity and, consequently, resolution, **Figure S4**), suggesting a long permanence time of our AISe NCs in the vascular system. Note that under identical experimental conditions (including exposure time) imaging of the vasculature was not possible using commercial Ag_2S NPs. Moreover, the time course of the fluorescence signal generated by AISe NCs and Ag_2S NPs is completely different. This becomes evident when observing the trend of the fluorescence intensity generated at the liver and at the femoral vessels (**Figure 3B**). For Ag_2S NPs, the NIR intensity decreased at both locations to 40-45% of the maximum value over the course of 3 h. On the other hand, the signal coming from AISe NCs at the liver increased over time, and the intensity of the emission at the femoral vessels only decreased by 15% 3 h after injection. This prolonged imaging of the vasculature via FI is not common and it was ascribed to the unique combination of bright emission and surface modification of the nanostructures. Firstly, the encapsulation in PEGylated phospholipids is expected to minimize the formation of a protein corona around the AISe NCs.[25] In addition, the surface modification with maleimide was shown to induce a strong interaction with cell membranes via surface

9

thiols.[26] Therefore, specific interaction with cellular components of the blood vessels (mainly epithelial cells) can contribute to the extended permanence time within the vascular system.[27]

Motivated by the apparent advantage of using AISe NCs in vasculature imaging, we applied the principal components analysis (PCA) to the set of *in vivo* images obtained in the time frame of the experiment.[28] Our goal was to check if a sharper distinction between the veins/arteries and the surrounding tissues could be achieved. The rationale for using PCA is that this analysis converts a set of observations based on certain variables into another set of linearly uncorrelated new variables ordered according to their importance.[29] A detailed description of the procedures applied to our set of data is described in Supporting Information. Hence the pixels containing static or slowly variable signals (highly correlated across the time frames) could be separated from the ones with faster dynamics.[30] Therefore, in some components (PCX, with $X \geq 1$), certain organs could be more highlighted than others. Since the accumulation of the NCs was preferential at the liver, it comes as no surprise that this organ would be in the spotlight in the first components (**Figure S5**).[5d] For our purposes, however, PC3 is particularly interesting. We selected a representative vessel in the right ventral region (white circle in **Figure 3C**, left) and analyzed the projection of the pixels corresponding to the vessel onto PC3 (**Figure 3C**, right). The thickness of the vessel can be retrieved from a Gaussian fit of the signal and considering the full width at half maximum of the fitting curve (260 μm in this case). What is even more interesting is that, aside from a difference in the magnitude (observed in PC1 and PC2 too), there is also a change in the sign of the signal arising from the vessel and the surrounding tissue. This means that for at least one of the new linearly independent variables, the behavior presented by the vessels was in direct opposition to the one of the surrounding tissues. For this reason, the vessels become markedly visible in this component of the PCA (**Figure 3C**). Moreover, although PC1 and PC2 did not highlight the vasculature as well as PC3, the contrast offered by them was still remarkable (**Figure S5**). Overall, the analysis suggests a good capability of the AISe NCs to work as a contrast agent in

enhanced angiography. The extended permanence time of AISe NCs in the vasculature make them suited for applications in angiography and detection of local deficiencies in blood perfusion caused by, for instance, stroke.[5g, 31]

Further confirmation of the capability of the developed AISe NCs to act as effective vasculature markers, was obtained from *ex vivo* NIR images (**Figure 4**). Strong NIR signal was observed in correspondence of blood vessels in the organs. As it can be observed, the vasculature is highlighted in a wide number of organs, such as dorsal skin and muscle, the kidneys, and even the brain. Regarding the two latter organs, the internal vasculature of the kidneys is well resolved in their sagittal and transversals sections, while the characteristic Polygon of Willis is observed prior to any dissection in the ventral part of the brain. To further confirm this preferential accumulation in the vasculature, we dissected the aorta, observing an increased signal at the vessel compared to the superficial perivascular fat, similarly to what observed *ex vivo* for the femoral vessels in the right hindlimb. Depending on the analysed part of the animal, the contrast achieved with AISe NCs varies, with some vessels (e.g., those in the muscle of the hindlimb and in the skin) being better discerned than other (e.g., those in the kidneys), with an observed maximum ratio between the signal coming from the vessel and the surrounding tissue varying between 1.3 and 6.

Conclusion.

We have herein presented the first example of $AgInSe_2$-based contrast agent for fluorescence imaging in the second biological window. The emission of these nanoparticles is shifted towards longer wavelengths compared to the usual emission featured by $AgInSe_2$ due to an uncommon crystal structure, imparted by the Ag_2S-seed mediated synthesis that we adapted from the literature. Upon transfer to water with the aid of maleimide-bearing phospholipids, nanocapsules composed of several $AgInSe_2$ nanoparticles are formed, which feature high colloidal stability and lack of *in vitro* cytotoxicity. Their brighter emission and longer

permancence time within the vascular system compared to commercial Ag_2S nanoparticles make these nanocapsule an invaluable addition to the currently relatively limited library of contrast agents for near infrared fluorescence imaging. We also showed that the use of principal components analysis (PCA) allows observing more clearly the vasculature upon dynamical acquisition of fluorescence images after injection of $AgInSe_2$ nanocapsules.

Since the improvement of the performance of fluorescence imaging passes through the development of brighter contrast agents, this study represents an important step in this direction. While the developed $AgInSe_2$-based nanocapsules already perform better than commercially available Ag_2S nanoparticles, there is plenty of room for improvement via adjustment of the reaction conditions and exploitation of selective cation exchange procedures. Future research effort will be therefore directed along these lines.

Experimental Section.

Chemicals. Silver(I) oxide (AgO, 99.9% metal basis, Alfa Aesar), indium(III) acetate (In(OAc)3, 99.99% metal basis, Alfa Aesar), 1-dodecanethiol (DDT, ≥98%, Sigma-Aldrich), 1-octadecene (ODE, 90%, tech), oleylamine (OLA, 80-90%, Fisher), selenium powder (Se, powder, -100 mesh, ≥99.5% trace metals basis, Fisher), tributylphosphine (TBP, 95%, Fisher); tetrachloroethylene (TCE, 99%, extra pure), acetone (≥99%, Fisher); 1,2-distearoyl-sn-glycero-3-phosphoethanolamine-N-[maleimide(polyethylene glycol)-2000] (ammonium salt) Maleimide (DSPE-PEG2000-MAL), Avanti), acetone (≥99%, Fisher). All chemicals were used as received.

Synthesis of AISe NPs. The synthesis of AISe NPs was performed according to a previously reported procedure.4 A Se precursor solution was initially prepared dissolving 0.4 mmol (31.6 mg) of Se in 0.1 mL of TBP and 0.3 mL of ODE. In the meantime, 0.05 mmol (6.2 mg) of AgO and 0.05 mmol (14.6 mg) of In(OAc)3 were added to a mixture of 0.25 mL of DDT and 5 mL of ODE. The mixture was degassed under vacuum for 30 min at 90 °C, followed by addition of

0.25 mL of OLA. The mixture was degassed for further 30 min under vacuum, backfilled with Ar, stirred until it became clear and the temperature was then set to 190 ℃. Upon reaching the target temperature, 0.2 mL of Se precursor was swiftly injected and the solution was maintained at 190 ℃ for 90 min. The product was precipitated by adding acetone, followed by centrifugation at 3,820 rcf for 30 min. The supernatant was discarded, and the pellet redispersed in 3 mL of TCE. The sample was stored at -20 ℃ for further use.

Transfer of AgInSe$_2$ NPs to aqueous media. Typically, 0.2 mL of AISe NPs in TCE (0.5 mg/mL) were transferred in a 1.5-mL centrifuge tube and precipitated with 1 mL of methanol. The NPs were collected via centrifugation at 11,093 rcf for 2 min. The precipitate was redispersed in 0.5 mL of chloroform and sonicated for 3 min. Meanwhile, 20.0 mg of DSPE-PEG2000-MAL was dissolved in 1.5 mL of chloroform in a 50-mL round-bottom flask and sonicated for 3 min. The dispersion of AgInSe$_2$ in chloroform was added to the solution of DSPE-PEG2000-MAL and sonicated for 2 min at room temperature. The chloroform was slowly evaporated at room temperature with the aid of a rotary evaporator to form a thin film on the wall of the flask. The rehydration of the film was performed adding 3 mL of water (or PBS 1x) followed by sonicating for 3 min, which yielded the final AISe nanocapsules.

Characterization. The morphology and size of the NPs and NCs was investigated using a transmission electron microscope (TEM, JEM1400 Flash (JEOL) microscope). The optical extinction spectra were recorded at room temperature with a UV-vis-NIR spectrophotometer (Perkin Elmer Lambda1050) using a 1-nm step in the 400-2000 nm range. Infrared spectra were obtained in transmission mode on a Spectrum Two instrument (Perkin Elmer) in the 450–4000 cm-1 range with 4 cm-1 resolution, preparing KBr tablets containing 1 wt% of the analyzed material. Lifetime measurements were performed by using an Optical Parametric Oscillator (Quanta Ray) pumped by a frequency tripled Nd: YAG laser operating at 355 nm. The Optical Parametric Oscillator operates at 800 nm and provides 10-ns pulses with an average energy of 0.2 J and with a repetition rate of 10 Hz. For temperature-dependent studies, a cuvette

containing the AISe NCs dispersion was placed in a qpod 2e (Quantum Northwest, Inc.), using an 850-nm long-pass filter (Thorlabs FEL850) in the emission path. The emitted radiation was spectrally sorted by a high-brightness monochromator (Shamrock 163, Andor) and detected with an infrared photomultiplier (Hamamatsu H1033C). To record the photoluminescence decay curves, the photomultiplier was connected to a digital oscilloscope (Le Croy Wave Runner 500). Powder X-ray diffraction (PXRD) measurement was performed on a Rigaku D/max-γB diffractometer working in the Bragg-Brentano geometry (θ-2θ) with a step of 0.03° in the 20-60° range. The hydrodynamic diameter and Z-potential were measured at different temperatures with a Zetasizer Ultra (Malvern Panalytical, Ltd.) using a 1-cm cuvette containing 0.5 mg/mL dispersions in TCE, water and PBS.

Cytotoxicity tests. The HeLa human cervical epithelial cell line was grown in Dulbecco's Modified Eagle's Medium (DMEM, Gibco, Paisley, Scot- land, UK) supplemented with fetal calf serum (FCS 10%, Gibco) and 0.5% of antibiotics (penicillin G [10,000 U/mL] and streptomycin sulfate [10,000 mg/mL] (Gibco)). Cells were grown in a Thermo Scientific Midi 40 CO2 Incubator (Thermo Fisher Scientific Inc.) with a 5% CO_2 atmosphere, a 95% relative humidity and a constant temperature of 37 ℃.

The viability of HeLa cells exposed to AISe NCs was analyzed by the MTT assay.[32] Twenty-four hours after appropriate treatments with AISe NCs, 3-(4,5-dimethylthiazol-2-yl)-2,5-diphenyltetrazolium bromide (MTT) solution was added to each well at a concentration of 0.5 ng/mL, and plates were incubated at 37 ℃ for 2 h. The resulting formazan crystals were dissolved by the addition of DMSO and absorbance was measured at 540 nm. Cell viability was estimated as a percentage relative to the mean absorption obtained from control cells (not incubated with the AISe NCs; 100% viability).

Imaging system. NIR-II in vivo and ex vivo images were obtained with an InGaAs NIR camera (ZephIRTM 1.7). A fibre-coupled diode laser operating at 808 nm was used as excitation source (LIMO30-F200-DL808). The illumination power density was controlled by adjusting

the diode current and set to 50 mW/cm^2 (a low power density that prevented excessive tissue heating and subsequent drying) and the laser height was adjusted to illuminate the whole animal. A short-pass filter (Thorlabs FES 850) was placed immediately in front of the laser fiber to minimize specular and diffuse reflection effects. Additionally, 3 long-pass filters (Thorlabs FEL850) were used to minimize tissue autofluorescence signal.

Animal handling. In vivo experiments were approved by the regional authority for animal experimentation of the Comunidad de Madrid and were conducted in agreement with the Universidad Autónoma de Madrid (UAM) Ethics Committee, in compliance with the European Union directives 63/2010UE and Spanish regulation RD 53/2013. For this study, 2 CD1 female mouse (24-weeks old, weighing 45 g) bred at the animal facility of UAM were used. The mouse was first shaven completely with depilatory cream to minimize autofluorescence derived from hair. Then, the animal was anesthetized prior to the imaging experiments in an induction chamber with a continuous flow of 3% isoflurane (Forane, AbbVie Spain, S.L.U) and 2 L/min of 100% O$_2$ until loss of righting reflex was confirmed and breathing rhythm was significantly slowed down. Anaesthesia was maintained throughout the experiments by means of facemask inhalation of 1.5% isoflurane and 0.5 L/min of O$_2$. Throughout the experiment, the core body temperature was monitored with a rectal probe and kept at 36 ± 1 °C using a heating pad.

In vivo **fluorescence imaging.** With the animal deeply anesthetized, we administrated 150 μL of a 1-mg/mL dispersion of AISe NCs in PBS 1x via retro-orbital injection. Six videos of 5 min each, with a non-irradiation period of 1 min in between to minimize laser-induced animal heating, were obtained for the first 36 min. A second set of photos were obtained acquiring 1 photo every 10 min for the next 150 min. To perform Principal Component Analysis (PCA), the image frames obtained in the first 10 min after injection of AISe Ncs were loaded into an array using MATLAB software and the princomp function was used.

Ex vivo **fluorescence imaging.** After 3 h of *in vivo* imaging, the animal was immediately euthanized by beheading after induction of deep anaesthesia with isoflurane under a constant

oxygen flow rate of 2 mL/min and a concentration of 4% of isoflurane. The organs were removed and washed thoroughly with 0.9% NaCl solution at room temperature. The time between sacrifice and imaging was shorter than 5 min.

<div align="right">

Received: ((will be filled in by the editorial staff))
Revised: ((will be filled in by the editorial staff))
Published online: ((will be filled in by the editorial staff))

</div>

References

[1]   E. Ximendes, A. Benayas, D. Jaque, R. Marin, *ACS Nano* **2021**, DOI: 10.1021/acsnano.0c08349.

[2]   a) S. L. Jacques, *Phys. Med. Biol.* **2013**, 58, R37; b) A. Bashkatov, E. Genina, V. Kochubey, V. Tuchin, *J. Phys. D: Appl. Phys.* **2005**, 38, 2543.

[3]   a) P. Reineck, B. C. Gibson, *Adv. Opt. Mater.* **2017**, 5, 1600446; b) G. Hong, A. L. Antaris, H. Dai, *Nature Biomedical Engineering* **2017**, 1, 0010; c) A. M. Smith, M. C. Mancini, S. Nie, *Nat. Nanotechnol.* **2009**, 4, 710; d) E. Hemmer, A. Benayas, F. Legare, F. Vetrone, *Nanoscale Horizons* **2016**, 1, 168.

[4]   E. Hemmer, N. Venkatachalam, H. Hyodo, A. Hattori, Y. Ebina, H. Kishimoto, K. Soga, *Nanoscale* **2013**, 5, 11339.

[5]   a) G. Hong, J. C. Lee, A. Jha, S. Diao, K. H. Nakayama, L. Hou, T. C. Doyle, J. T. Robinson, A. L. Antaris, H. Dai, J. P. Cooke, N. F. Huang, *Circulation. Cardiovascular imaging* **2014**, 7, 517; b) J. Hu, D. H. Ortgies, E. Martín Rodríguez, F. Rivero, R. Aguilar Torres, F. Alfonso, N. Fernández, G. Carreño-Tarragona, L. Monge, F. Sanz-Rodriguez, M. d. C. Iglesias, M. Granado, A. L. García-Villalon, J. García Solé, D. Jaque, *Adv. Opt. Mater.* **2018**, 6, 1800626; c) J. Hu, D. H. Ortgies, R. Aguliar Torres, N. Fernández, L. Porto, E. Martín Rodríguez, J. García Solé, D. Jaque, F. Alfonso, F. Rivero, *Adv. Funct. Mater.* **2017**, 27, 1703276; d) K. Welsher, S. P. Sherlock, H. Dai, *Proc Natl Acad Sci U S A* **2011**, 108, 8943; e) D. J. Naczynski, M. C. Tan, M. Zevon, B. Wall, J. Kohl, A. Kulesa, S. Chen, C. M. Roth, R. E. Riman, P. V. Moghe, *Nat. Commun.* **2013**, 4, 2199; f) Y. Zhang, G. Hong, Y. Zhang, G. Chen, F. Li, H. Dai, Q. Wang, *ACS Nano* **2012**, 6, 3695; g) G. Hong, S. Diao, J. Chang, A. L. Antaris, C. Chen, B. Zhang, S. Zhao, D. N. Atochin, P. L. Huang, K. I. Andreasson, C. J. Kuo, H. Dai, *Nat. Photonics* **2014**, 8, 723.

[6]   D. Jaque, C. Richard, B. Viana, K. Soga, X. Liu, J. G. Solé, *Advances in Optics and Photonics* **2016**, 8, 1.

[7]   a) Y. Shen, H. D. A. Santos, E. C. Ximendes, J. Lifante, A. Sanz-Portilla, L. Monge, N. Fernández, I. Chaves-Coira, C. Jacinto, C. D. S. Brites, L. D. Carlos, A. Benayas, M. C. Iglesias-de la Cruz, D. Jaque, n/a, 2002730; b) D. Ruiz, B. del Rosal, M. Acebrón, C. Palencia, C. Sun, J. Cabanillas-González, M. López-Haro, A. B. Hungría, D. Jaque, B. H. Juarez, *Adv. Funct. Mater.* **2017**, 27, 1604629; c) D. Yan, Y. He, Y. Ge, G. Song, *Sensors and Actuators B: Chemical* **2017**, 240, 863; d) B. del Rosal, D. Ruiz, I. Chaves-Coira, B. H. Juárez, L. Monge, G. Hong, N. Fernández, D. Jaque, *Adv. Funct. Mater.* **2018**, 28, 1806088; e) H. D. A. Santos, E. C. Ximendes, M. d. C. Iglesias-de la Cruz, I. Chaves-Coira, B. del Rosal, C. Jacinto, L. Monge, I. Rubia-Rodríguez, D. Ortega, S. Mateos, J. GarcíaSolé, D. Jaque, N. Fernández, *Adv. Funct. Mater.* **2018**, 28, 1803924; f) C. Li, Y. Zhang, M. Wang, Y. Zhang, G. Chen, L. Li, D. Wu, Q. Wang, *Biomaterials* **2014**, 35, 393; g) D. H. Ortgies, Á. L. García-Villalón, M. Granado, S. Amor, E. M. Rodríguez, H. D. A. Santos, J. Yao, J. Rubio-Retama, D. Jaque, *Nano Res.* **2019**, 12, 749.

[8]   Y. Zhang, Y. Zhang, G. Hong, W. He, K. Zhou, K. Yang, F. Li, G. Chen, Z. Liu, H. Dai, Q. Wang, *Biomaterials* **2013**, 34, 3639.

[9]   a) H. D. A. Santos, I. Zabala Gutiérrez, Y. Shen, J. Lifante, E. Ximendes, M. Laurenti, D. Méndez-González, S. Melle, O. G. Calderón, E. López Cabarcos, N. Fernández, I. Chaves-Coira, D. Lucena-Agell, L. Monge, M. D. Mackenzie, J. Marqués-Hueso, C. M. S. Jones, C. Jacinto, B. del Rosal, A. K. Kar, J. Rubio-Retama, D. Jaque, *Nat. Commun.* **2020**, 11, 2933; b) D. Ruiz, M. Mizrahi, H. D. A. Santos, D. Jaque, C. M. S. Jones, J. Marqués-Hueso, C. Jacinto, F. G. Requejo, A. Torres-Pardo, J. M. González-Calbet, B. H. Juárez, *Nanoscale* **2019**, 11, 9194; c) L. M. Maestro, P. Haro-González,

17

B. Del Rosal, J. Ramiro, A. Caamano, E. Carrasco, A. Juarranz, F. Sanz-Rodríguez, J. G. Solé, D. Jaque, *Nanoscale* **2013**, 5, 7882.

[10] A. Ortega-Rodriguez, Y. Shen, I. Zabala Gutierrez, H. D. A. Santos, V. Torres Vera, E. Ximendes, G. Villaverde, J. Lifante, C. Gerke, N. Fernandez, O. G. Calderon, S. Melle, J. Marques-Hueso, D. Mendez-Gonzalez, M. Laurenti, C. M. S. Jones, J. M. Lopez-Romero, R. Contreras-Caceres, D. Jaque, J. Rubio-Retama, *ACS Appl Mater Interfaces* **2020**, 12, 12500.

[11] a) J.-Y. Chang, G.-Q. Wang, C.-Y. Cheng, W.-X. Lin, J.-C. Hsu, *J. Mater. Chem.* **2012**, 22, 10609; b) X. Hu, T. Chen, Y. Xu, M. Wang, W. Jiang, W. Jiang, *J. Lumin.* **2018**, 200, 189.

[12] S. E. Creutz, R. Fainblat, Y. Kim, M. C. De Siena, D. R. Gamelin, *J Am Chem Soc* **2017**, 139, 11814.

[13] D. Deng, L. Qu, Y. Gu, *Journal of Materials Chemistry C* **2014**, 2.

[14] M. A. Langevin, A. M. Ritcey, C. N. Allen, *ACS Nano* **2014**, 8, 3476.

[15] M. T. Ng, C. B. Boothroyd, J. J. Vittal, *J Am Chem Soc* **2006**, 128, 7118.

[16] a) B. A. Tappan, M. K. Horton, R. L. Brutchey, *Chemistry of Materials* **2020**, 32, 2935; b) T. Bai, S. Xing, C. Li, Z. Shi, S. Feng, *Chem Commun (Camb)* **2016**, 52, 8581.

[17] J. M. J. M. Ravasco, H. Faustino, A. Trindade, P. M. P. Gois, **2019**, 25, 43.

[18] T. Li, S. Takeoka, *Int. J. Nanomed.* **2014**, 9, 2849.

[19] O. S. Oluwafemi, B. M. M. May, S. Parani, N. Tsolekile, *Materials Science and Engineering: C* **2020**, 106, 110181.

[20] S. Kumar Panigrahi, A. Kumar Mishra, *Journal of Photochemistry and Photobiology C: Photochemistry Reviews* **2019**, 41, 100318.

[21] F. Wang, J. Wang, X. Liu, *Angew Chem Int Ed Engl* **2010**, 49, 7456.

[22] Y. Shen, J. Lifante, E. Ximendes, H. D. A. Santos, D. Ruiz, B. H. Juarez, I. Zabala Gutierrez, V. Torres Vera, J. Rubio Retama, E. Martin Rodriguez, D. H. Ortgies, D. Jaque, A. Benayas, B. Del Rosal, *Nanoscale* **2019**, 11, 19251.

[23] H. D. A. Santos, I. Zabala Gutierrez, Y. Shen, J. Lifante, E. Ximendes, M. Laurenti, D. Mendez-Gonzalez, S. Melle, O. G. Calderon, E. Lopez Cabarcos, N. Fernandez, I. Chaves-Coira, D. Lucena-Agell, L. Monge, M. D. Mackenzie, J. Marques-Hueso, C. M. S. Jones, C. Jacinto, B. Del Rosal, A. K. Kar, J. Rubio-Retama, D. Jaque, *Nat Commun* **2020**, 11, 2933.

[24] H. Santos, D. Ruiz, G. Lifante, C. Jacinto, B. Juarez, D. Jaque, *Nanoscale* **2017**, 9, 2505.

[25] a) T. Lima, K. Bernfur, M. Vilanova, T. Cedervall, *Scientific Reports* **2020**, 10, 1129; b) P. d. Pino, B. Pelaz, Q. Zhang, P. Maffre, G. U. Nienhaus, W. J. Parak, *Materials Horizons* **2014**, 1, 301.

[26] A. G. Torres, M. J. Gait, *Trends Biotechnol* **2012**, 30, 185.

[27] R. B. Huang, S. Mocherla, M. J. Heslinga, P. Charoenphol, O. Eniola-Adefeso, *Mol Membr Biol* **2010**, 27, 190.

[28] E. M. C. Hillman, A. Moore, *Nat. Photonics* **2007**, 1, 526.

[29] a) S. Wold, K. Esbensen, P. Geladi, *Chemometrics and Intelligent Laboratory Systems* **1987**, 2, 37; b) R. Vidal, Y. Ma, S. S. Sastry, in *Generalized Principal Component Analysis*, DOI: 10.1007/978-0-387-87811-9_2 **2016**, Ch. Chapter 2, p. 25.

[30] N. Le, S. Song, Q. Zhang, R. K. Wang, *Quant Imaging Med Surg* **2017**, 7, 654.

[31] a) R. Bhavane, Z. Starosolski, I. Stupin, K. B. Ghaghada, A. Annapragada, *Scientific Reports* **2018**, 8, 14455; b) F. C. Piccolino, L. Borgia, E. Zinicola, M. Iester, S. Torrielli, *Ophthalmology* **1996**, 103, 1837.
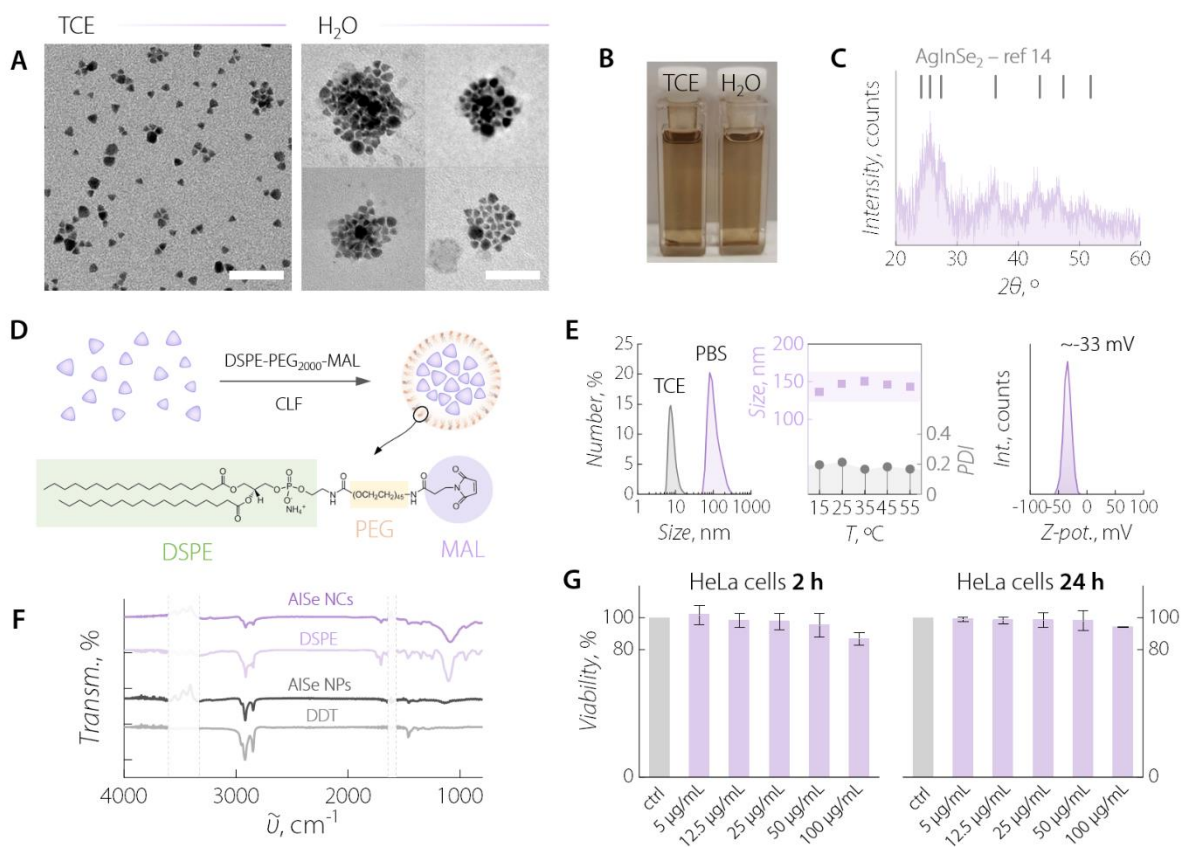
[32]

Figure 1. Characterization of the morphology, structure, surface chemistry, and cytotoxicity of AISe NPs and NCs. **A)** TEM images before and after phospholipid-assisted transfer to water. Scale bars are 50 nm. **B)** Optical image of a dispersion of AISe NPs in TCE and AISe NCs in water. **C)** PXRD pattern of AISe NPs, along with the position of the main reflections reported in ref 14 for the same material. **D)** Scheme of the encapsulation mechanism, along with the chemical structure of the DSPE-PEG$_{2000}$-MAL phospholipids used for preparing AISe NCs. **E)** DLS and Z-potential measurements performed on AISe NPs (in TCE) and AISe NCs (DLS in PBS 1x and Z-potential in water). The values reported for the hydrodynamic diameter of AISe NCs vs temperature are Z-average values given by the software. **F)** FTIR spectra of AISe NPs and AISe NCs, along with the spectra of pristine DDT and DSPE-PEG$_{2000}$-MAL. The areas shaded in white correspond to ranges where spurious signals originating during the background subtraction procedure are located. **G)** Cell viability tests performed on HeLa cells after 2 and 24 h of cell incubation at extracellular AISe NCs concentration between 5 and 100 µg/mL.
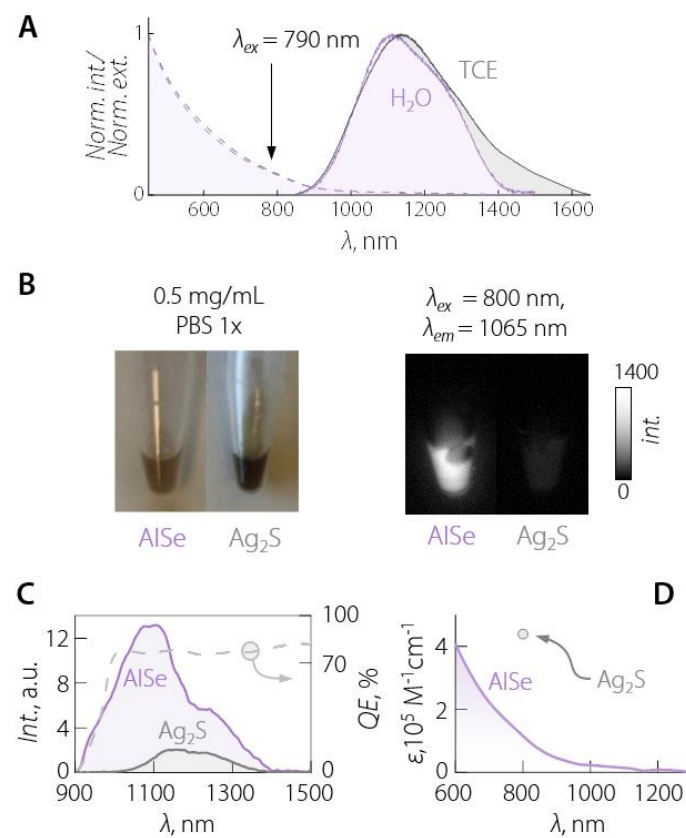
Figure 2. A) Absorption (dashed lines) and emission (solid lines, λ_{ex} = 790 nm) spectra of AISe NPs in TCE (grey) and AISe NCs in water (purple). **B)** Optical (left) and NIR-II (right) image of two centrifuge tubes containing a dispersion of AISe NCs and Ag_2S NPs (0.5 mg/mL). **C)** Comparison of the emission spectra obtained at the *in vivo* imaging setup. The response curve (quantum efficiency, QE) of the detector is also reported (dashed grey line). **D)** Calculated molar extinction coefficient of an AISe NCs dispersion in water (purple line) and the value for commercial Ag_2S NPs at 800 nm (grey dot) obtained from ref [9a].

Figure 3. A) Comparison of the performance of AISe NCs and commercial Ag$_2$S NPs as contrast agents: Picture of the CD1 female mouse before injection and time-course NIR images taken under 808-nm excitation at different time points after retro-orbital injection of 150 µL of a 1.0-mg/mL dispersion of either AISe NCs (top) or Ag$_2$S NPs (bottom) in PBS 1x. **B)** Comparison of the temporal evolution of the NIR signal at the liver (top) and at the femoral vessels (lower) of two mice injected with AISe NCs (purple) and Ag$_2$S NPs (grey) respectively. The corresponding areas for the mouse injected with AISe NCs are also indicated. **C)** Third component (PC3) of the PCA and intensity profile measured along the white arrow. Note how the signal passes from positive to negative values from the surrounding tissues to the vessel. The thickness of the vessel (in orange) was obtained as the full width at half maximum of the Gaussian fit (dashed black line) to the data.
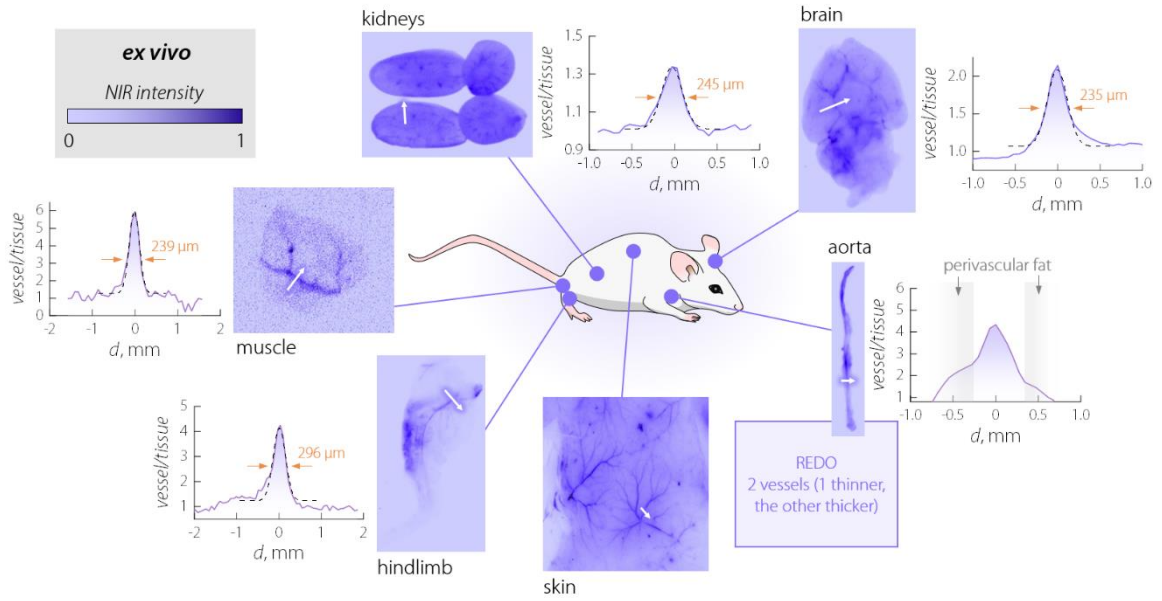
21

Figure 4. *Ex vivo* NIR images of selected tissues along with the ratio between the signal arising from the vessel and the surrounding tissue calculated along the white arrows. The thickness of the vessels, obtained as the full width at half maximum of a Gaussian fit (dashed black lines), is indicated in orange. In the case of the aorta, this analysis is challenging; therefore, the areas occupied by the perivascular fat are shaded in grey and the ratio is calculated versus the background of the image.

Supporting Information

In vivo near-infrared imaging using ternary selenide semiconductor nanoparticles with uncommon crystal structure.

Jingke Yao, José Lifante, Paloma Rodríguez, María de la Fuente-Fernández, Francisco Sanz-Rodríguez, Dirk H. Ortgies, Erving Ximendes, Daniel Jaque,* and Riccardo Marin*

Table of contents.

Size distribution of AgInSe$_2$ nanoparticles before transfer to water.
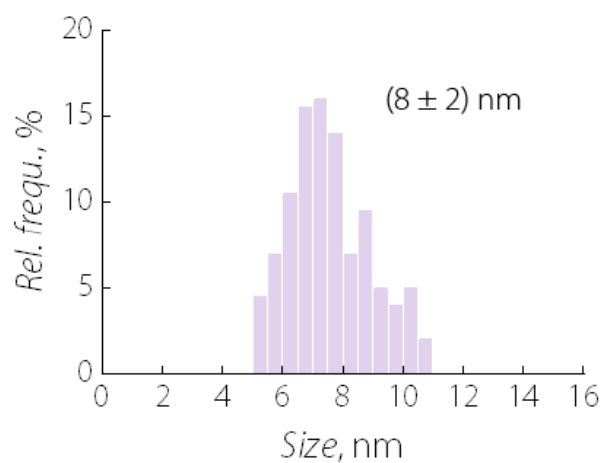

Figure S1. Size distribution for AgInSe$_2$ nanoparticles (NPs) obtained from TEM observations.

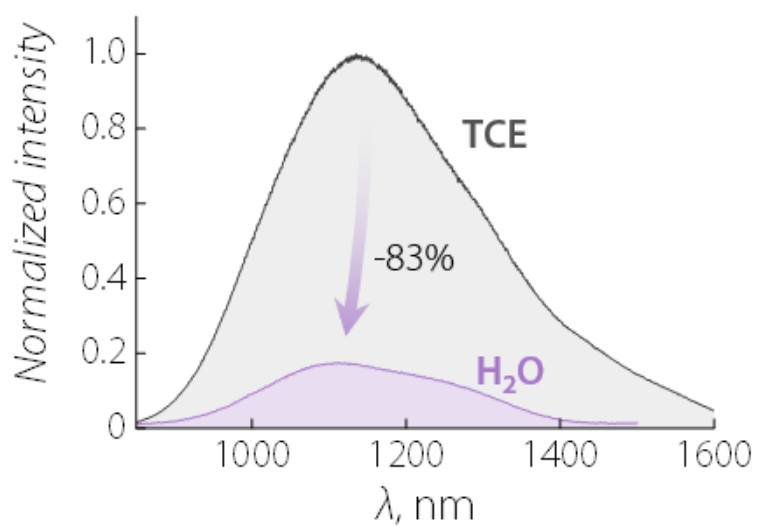**Comparison of emission intensity before and after transfer to water.**

Figure S2. Comparison of the emission spectra obtained under 790-nm excitation for AISe NPs in TCE (grey) and AISe NCs in water (purple).

Concentration and molar extinction coefficient calculation for AgInSe₂ nanocapsules.

To determine the molar extinction coefficient of the $AgInSe_2$ nanocapsules (AISe NCs), an extinction spectrum was recorded in water on a dispersion at a mass concentration ([mass]) of 0.25 mg/mL. To estimate the molar concentration of this dispersion, the following considerations were made.

The single nanoparticles composing the NCs have a tetrahedral shape with an edge (a) of 8 nm. The volume of the single nanoparticle was calculated to be 60 nm³ according to the following formula:

$$V_{NP} = \frac{a^3}{6\sqrt{2}} \qquad (S1)$$

To calculate the density of the material, we considered that orthorhombic $AgInS_2$ (which is isostructural to our $AgInSe_2$) has four molecular units in the unit cell ($Z = 4$). Considering a molecular weight (MW) of $AgInSe_2$ of 380.6 and a unit cell volume (V_{cell}) of 0.4243 nm³ (as obtained by the group of Vittel),[1] the density (d) of orthorhombic $AgInSe_2$ was estimated to be 5.96 g/cm according to the following formula:

$$d = \frac{Z \cdot MW \cdot 1.66 \cdot 10^{-24}}{V_{cell}} \qquad (S2)$$

Where $1.66 \cdot 10^{-24}$ g is the value of the atomic mass unit (Dalton).
Using V_{NP} and d, the mass (m_{NP}) of a single nanoparticle was calculated to be $3.59 \cdot 10^{-19}$ g. Therefore, the molar concentration of the AISe NCs dispersion is given by:

$$[M] = \frac{[mass]}{m_{NP} \cdot N_A} \qquad (S3)$$

Where N_A is the Avogadro's number ($6.022 \cdot 10^{23}$).
For a concentration of 0.25 mg/mL, the molar concentration found was of $1.15 \cdot 10^{-6}$ mol/L. The data obtained from the absorption spectrometer was divided by this value to obtain the graph in **Figure 2D** of the main manuscript.

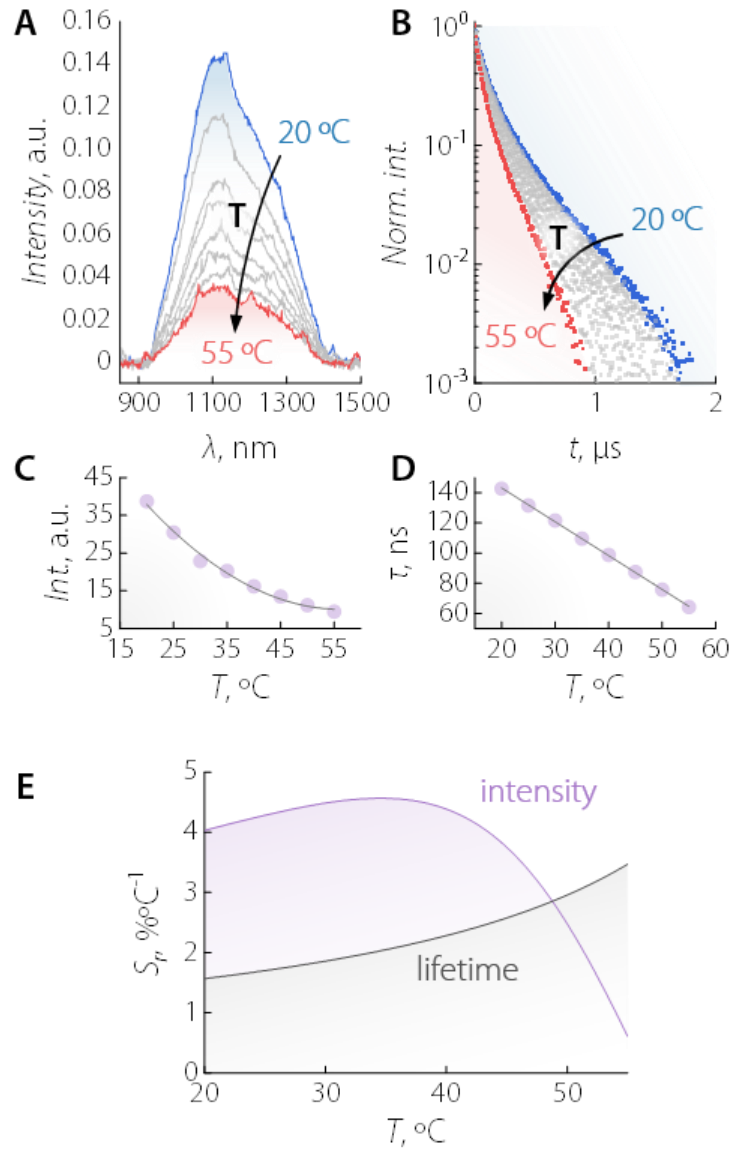**Thermometric performance of AgInSe₂ nanocapsules.**

Figure S3. A) Emission spectra and **B)** photoluminescence decay curves of a AISe NCs dispersions obtained as a function of temperature under 800-nm excitation. **C)** Integrated emission intensity and **D)** average lifetime as a function of the temperature of the dispersion. The solid lines are respectively the parabolic and linear fit of the data. **E)** Relative thermal sensitivity obtained from the fit of the data in **C** (purple line) and **D** (grey line).

The relative sensitivity was obtained according to the following equation:[2]

$$S_r = \frac{1}{\Delta}\frac{\partial \Delta}{\partial T}$$

(S4)

Where Δ is the either the integrated intensity of the NIR emission or the average lifetime obtained from the integration of the normalized decay curves.
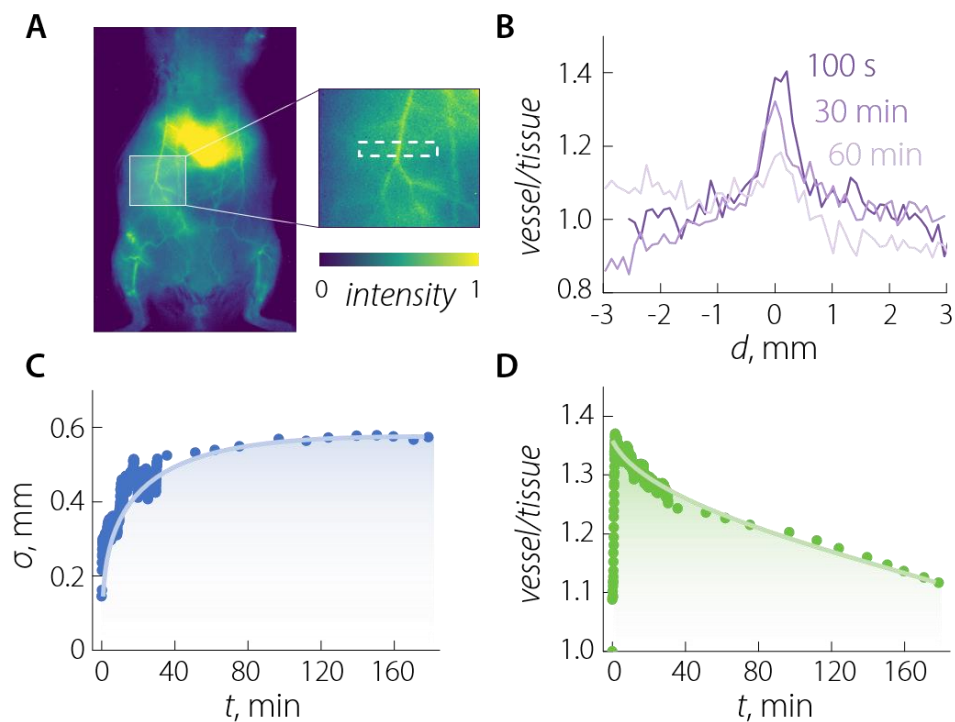
Temporal evolution of contrast and resolution.

Figure S4. A) NIR image obtained 15 min after administration of AISe NCs and zoom-in of the area where the profile of the blood vessel was monitored (white dashed box). **B)** Profile of the intensity ratio between the signal from the vessel and from the surrounding tissue at three different time points (100 s, 30 min, 60 min). Temporal evolution of **C)** the width at half maximum (σ) obtained of the Gaussian fit of the profiles and **D)** the vessel-to-tissue intensity ratio. Note that a broadening of the peak can be correlated qualitatively to a loss of spatial resolution.

Principal Components of dynamically acquired fluorescence images.

For every pixel in the 150 fluorescence images (512×640 of resolution) acquired after the intravenous injection of NPs, the evolution of its intensity could be represented by a vector of dimension 150. Thus, each of the 150 coordinates would correspond to the intensity value at an instant t = (m-1)×Δt, where m is a natural number between 1 and 150 and Δt is the integration time used in the measurement. Under this perspective, the experimental dataset is no longer viewed as a list of 150 matrices of dimensions 512×640 but instead as a single matrix of 327680 lines and 150 columns. In other words, if the m-th luminescence image is:

$$I(m) = \begin{pmatrix} I_{1,1}^m & \cdots & I_{1,640}^m \\ \vdots & \ddots & \vdots \\ I_{512,1}^m & \cdots & I_{512,640}^m \end{pmatrix}$$

Then the unified matrix is given by:

$$N = \begin{pmatrix} I_{1,1}^1 & \cdots & I_{1,1}^{150} \\ I_{1,2}^1 & \cdots & I_{1,2}^{150} \\ \vdots & \cdots & \vdots \\ I_{512,640}^1 & \cdots & I_{512,640}^{150} \end{pmatrix}$$

To pre-process the data, we compute the means, A_i, and the standard deviations, σ_i, of each of the 150 columns. With these values we then calculate the following matrix:

$$M = \begin{pmatrix} \dfrac{\left(I_{1,1}^1 - A_1\right)}{\sigma_1} & \cdots & \dfrac{\left(I_{1,1}^{150} - A_{150}\right)}{\sigma_{150}} \\ \dfrac{\left(I_{1,2}^1 - A_1\right)}{\sigma_1} & \cdots & \dfrac{\left(I_{1,2}^{150} - A_{150}\right)}{\sigma_{150}} \\ \vdots & \cdots & \vdots \\ \dfrac{\left(I_{512,640}^1 - A_1\right)}{\sigma_1} & \cdots & \dfrac{\left(I_{512,640}^{150} - A_{150}\right)}{\sigma_{150}} \end{pmatrix}$$

The Principal Component Analysis is then started by calculating the covariance matrix (dimensions: 150 x 150) corresponding to the matrix M. Its value at the i-th row and j-th column is given by:

$$Cov_{ij} = \sum_{q=1}^{327680} \frac{\left(M_{q,i} - \rho_i\right)\left(M_{q,j} - \rho_j\right)}{327679}$$

where $\rho_i = \sum_{j=1}^{327680} M_{j,i}$.

Once the Covariance Matrix is obtained, its eigenvectors (principal components) and eigenvalues are calculated. If an eigenvalue is large, then the corresponding principal component is important in describing the pharmacokinetics of the NPs. However, if the eigenvalue is near zero, that principal component is relatively unimportant. Once the eigenvectors are found, we use their 150 coordinates to compute linear combinations of the original 150 images according to:

$$P_k = \sum_{r=1}^{150} v_r^k (I(r) - \bar{I}_r)/\sigma_r$$

where v_r^k is the r-th coordinate value of the k-th eigenvector and $\bar{I}_r$ is an image whose pixels values are all equal to A_r. We call P_k the projection of the experimental data on the k-th principal component. As representative examples, we include the first three projections in Figure S5.
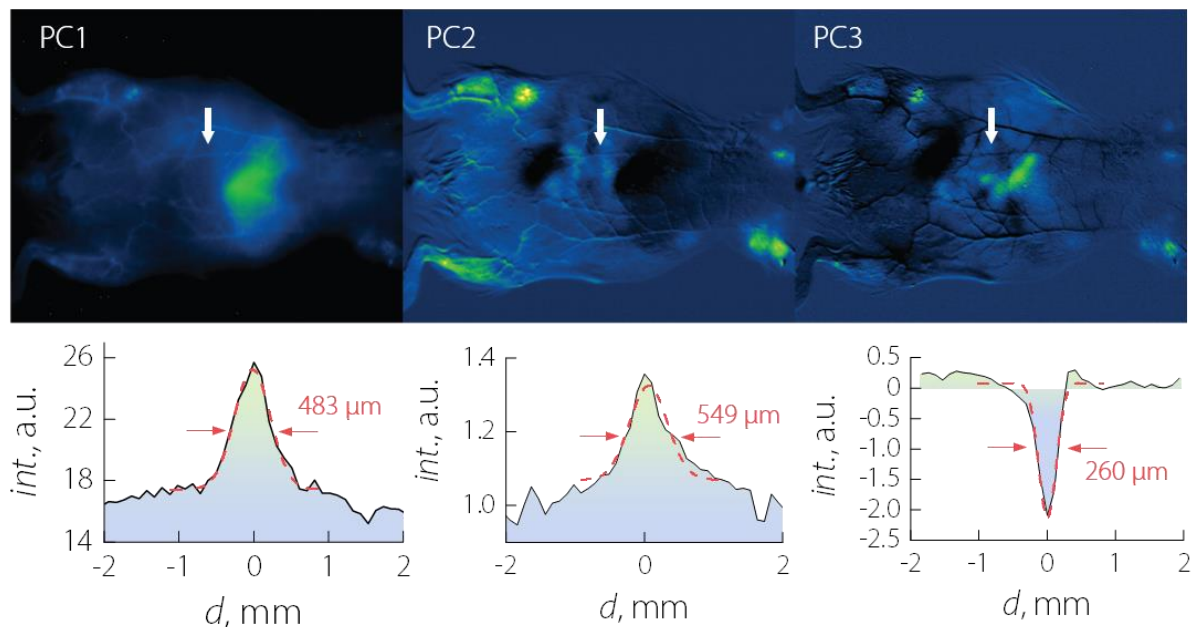

Figure S5. The first three components of dynamically acquired *in vivo* fluorescence images as obtained through PCA analysis in MATLAB.. The projections of a line (passing through a blood vessel) in each of these components are found at the bottom part of the figure, along with the Gaussian fit of the signal coming from the vessel. PC3 allows a better observation of the vessels, as inferred by the strong contrast and the higher resolution achieved in this figure. The better resolution can be appreciated by the narrower Gaussian fit of the signal coming from the vessel in this component (260 µm of full width at half maximum) in comparison with the larger values obtained for PC1 (483 µm) and PC2 (549 µm).

References.

1. M. T. Ng, C. B. Boothroyd, J. J. Vittal, *J. Am. Chem. Soc*. **2006**, *128*, 7118.
2. S. A. Wade, S. F. Collins, G. W. Baxter, *J. Appl. Phys. 2003*, *94*, 4743.